

Check for updates

# Active Transport of Biomimetic Cascaded Nanozymes Across Blood-Brain Barrier to Scavenge ROS and Alleviate Neuroinflammation Against Cerebral Ischemia Reperfusion Injury

Yuqi Wu, Jie Xu, Xinxin Wang, Han Li, Fan Wu, Jian Ruan, Dong Chen, Jianpeng Sheng, Dingcheng Zhu,\* Junqiu Liu,\* and Baiheng Wu\*

The rational design of potent antioxidative agents with active transport across blood-brain barrier (BBB) is critically required for mitigating ischemic reperfusion-induced reactive oxygen species (ROS)-mediated neuroinflammation and neural injury in ischemic stroke therapy. Herein, a biomimetic nanozyme is engineered by integrating copper and selenium, key catalytic sites of natural antioxidant superoxide dismutase and glutathione peroxidase, into mesoporous polydopamine scaffolds (mPDA-Cu/Se), yielding cascaded enzymatic activities for robust ROS scavenging. This nanozyme is further functionalized with a BBB-penetrating peptide RVG29 and biocompatible red blood cell membrane (T-mPDA-Cu/Se) for enhanced BBB penetration and ischemic neuronal tissues accumulation in a transient middle cerebral artery occlusion rat model, where it effectively mitigates oxidative damage and neuron apoptosis. T-mPDA-Cu/Se also mitigates neuroinflammation-induced injury by inhibiting astrocyte activation, microglia pro-inflammatory polarization, and proinflammatory cytokines secretion, thus achieving reduced infarct volume and improved neuronal recovery without noticeable systemic toxicity. Collectively, this study provides a promising neuroprotective approach against reperfusion-induced neuron injury in ischemic stroke.

### 1. Introduction

Ischemic stroke, constituting ≈87% of strokes, remains a lethal cerebral disease threatening global health.[1-3] Over 60% of survivors develop chronic disabilities poststandard thrombectomy or thrombolysis treatment, primarily due to secondary cerebrovascular/neural damage.[4-6] Pathophysiologically, hypoxia-reoxygenation induces mitochondrial electron leakage and a burst of reactive oxygen species (ROS), such as hydrogen peroxide (H2O2) and superoxide anion (O2 •-), that mediate oxidative neuronal injury.[7-9] Damage-associated molecular patterns released from necrotic neurons potentiate ROS-induced activation of astrocytes and microglia proinflammatory polarization, triggering inflammatory cytokine storm.[10,11] These inflammatory mediators (including ROS and cytokines) not only amplify oxidative neuronal damage, establishing a self-

Y. Wu, J. Xu, X. Wang, D. Zhu, J. Liu, B. Wu
Key Laboratory of Organosilicon Chemistry and Material Technology
Ministry of Education
Zhejiang Key Laboratory of Organosilicon Material Technology
College of Material, Chemistry and Chemical Engineering
Hangzhou Normal University
Hangzhou, Zhejiang 311121, P. R. China
E-mail: zhudc@hznu.edu.cn; junqiuliu@hznu.edu.cn;
bhwu@hznu.edu.cn
H. Li, J. Ruan, D. Chen

H. Li, J. Ruan, D. Chen
Department of Medical Oncology
The First Affiliated Hospital
School of Medicine
Zhejiang University
Hangzhou, Zhejiang 310003, P. R. China

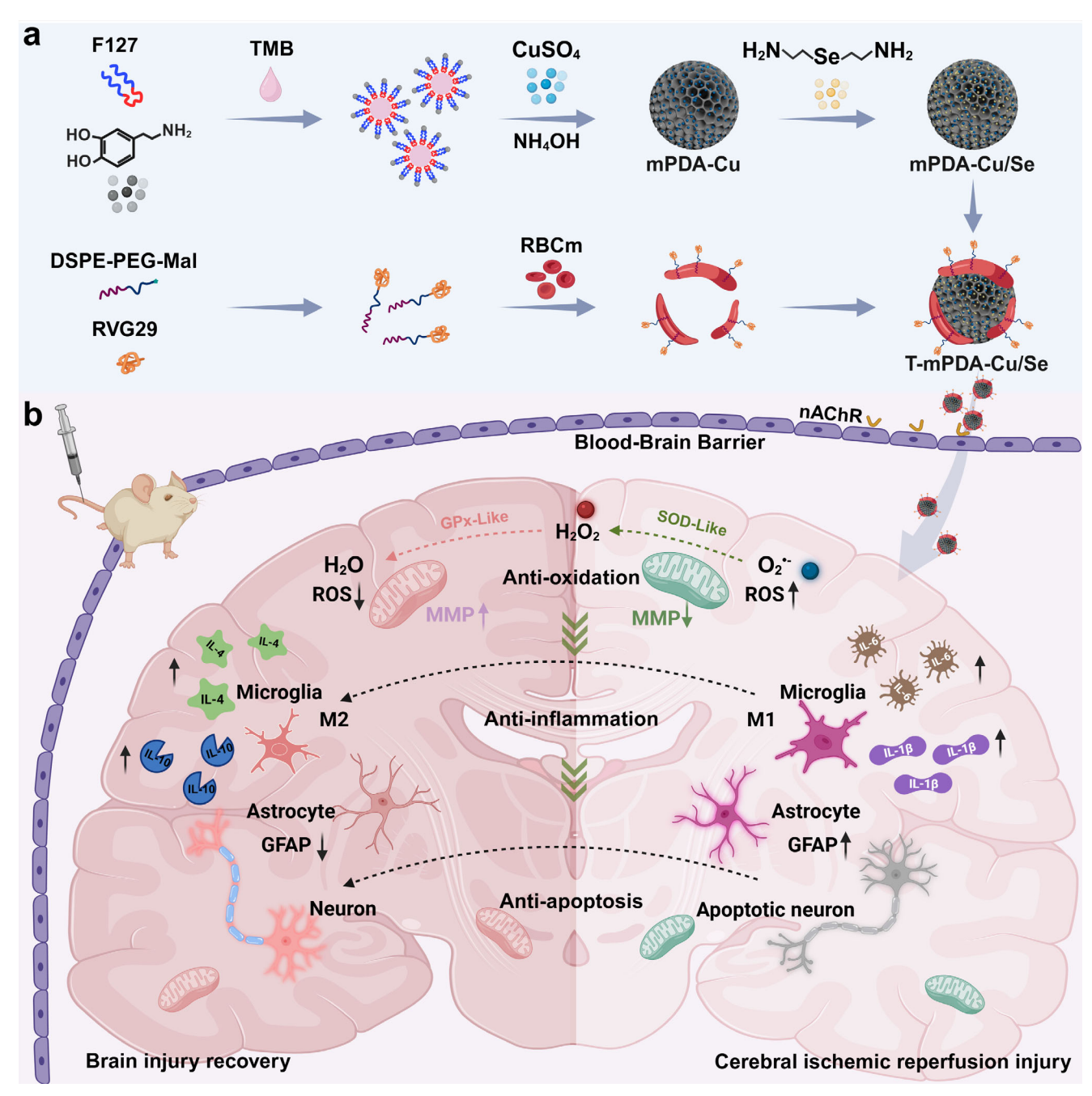
The ORCID identification number(s) for the author(s) of this article can be found under https://doi.org/10.1002/adfm.202520000

DOI: 10.1002/adfm.202520000

F. Wu
Department of Neurosurgery
The First Affiliated Hospital
School of Medicine
Zhejiang University
Hangzhou, Zhejiang 310003, P. R. China
J. Sheng
Chinese Institutes for Medical Research
Capital Medical University
Beijing 100020, P. R. China

16163028, 0, Downloaded from https://advanced.onlinelibrary.wiley.com/doi/10.1002/adfm.202520000 by Hangzhou Normal University, Wiley Online Library on [10/11/2025]. See the Terms

on Wiley Online Library for rules of use; OA articles are governed by the applicable Creative Commons



Scheme 1. Schematic illustration of synthesis and therapeutic mechanism of T-mPDA-Cu/Se for CIRI. a) Cu/Se dual element doped mPDA mimics SOD and GPx activities, while coating with RVG29 peptide functionalized RBCm enables efficient BBB transverse and accumulation in ischemic brain regions. b) The nanozyme system alleviates CIRI by scavenging ROS, suppressing astrocyte- and microglia-induced neuroinflammation, and preventing neuronal apoptosis.

reinforcing neuroinflammatory cycle, but also disrupt bloodbrain barrier (BBB) integrity. Although clinically approved edaravone demonstrates neuroprotection in acute ischemic stroke through ROS scavenging, it, its utility is constrained by unsatisfactory pharmacokinetics (9 min half-life) and inefficient BBB permeability. These limitations underscore the demand for novel neuroprotectants integrating potent ROS elimination, high biocompatibility, and enhanced BBB transverse capabilities.

Antioxidant nanozymes exhibit superior stability, tunable catalytic activity, and cost-effectiveness, with validated therapeutic efficacy against neurodegenerative disorders and ischemia-reperfusion injuries.<sup>[17-22]</sup> Cascade nanozymes surpass a single-activity system in orchestrating antioxidant and anti-inflammatory responses.<sup>[23]</sup> However, the BBB poses a major challenge for achieving sufficient nanozyme accumulation in ischemic regions.<sup>[24,25]</sup> Passive translocation across damaged

1616328, D. Downloaded from https://advanced.onlinelibrary.wiley.com/doi/10.1002/adfm.202320000 by Hangzhou Normal University, Wiley Online Library on [10/11/2025]. See the Terms and Conditions (https://onlinelibrary.wiejc.com/terms-and-conditions) on Wiley Online Library for rules of use; OA articles are governed by the applicable Creative Commons License

ischemic BBB causes limited availability and uncontrollable distributions.[26,27] and invasive intraventricular injection risks hemorrhage and pain.[28,29] Consequently, active transport via cerebral endothelial transcytosis dramatically enhances BBB permeability with high safety. In addition, conventional PEGylation strategies reduce reticuloendothelial clearance of nanozymes to improve bioavailability, but simultaneously inhibit their interactions with cerebral endothelia, compromising BBB traversing. Red blood cell membrane (RBCm) coating enhances biocompatibility, prolongs circulation, and delivers membrane-anchored antioxidants (e.g., vitamin E) without impeding BBB penetration of nanoparticles.[30,31] Therefore, integrating cascade catalysis and active transport across BBB within one individual nanosystem remains critical for cerebral ischemia-reperfusion injury (CIRI) therapy. Studies regarding CIRI treatments are summarized in Table S1 (Supporting Information).

Herein, we engineered T-mPDA-Cu/Se, a hierarchical nanozyme embedding superoxide dismutase (SOD)-mimetic copper (Cu) and glutathione peroxidase (GPx)-mimetic selenium (Se) within the mesoporous polydopamine (mPDA) scaffold (Scheme 1a). The ROS produced after reperfusion was eliminated efficiently by the cascade SOD-GPx catalytic activities of the nanozymes, demonstrating exceptional neuroprotection against oxygen-glucose deprivation/reoxygenation (OGD/R)-induced apoptosis of PC-12 cells. The engineered nanoplatform combined RVG29 BBB-penetrating peptide with RBCm coating, achieving targeted ischemic brain accumulation through receptor-mediated transcytosis while evading immune clearance. In transient middle cerebral artery occlusion (tMCAO) rat models, T-mPDA-Cu/Se that was accumulated in ischemic neuronal tissues efficiently attenuated neuronal oxidative damage, suppressed astrocytic/microglial activation, downregulated proinflammatory cytokines, and reduced infarct volume, exhibiting superior neuroprotection with biosafety (Scheme 1b). Given its excellent ROS scavenging and the ability to accumulate in the ischemic brain, our biocompatible nanozyme may lay the foundation for more effective treatment of ischemic stroke.

### 2. Results and Discussion

# 2.1. Preparation and Characterization of the Biomimetic T-mPDA-Cu/Se Nanozyme

mPDA was employed as the scaffold to integrate cascade enzymatic capabilities, leveraging the versatile chemistry of dopamine and the highly porous structure. [32,33] By optimizing the synthesis conditions (Figure S1, Supporting Information), mPDA nanoparticles with a uniform particle size of  $103.9 \pm 9.3$  nm were synthesized via an ammonium-catalyzed, Pluronic F127/1,3,5-trimethybenzene-based microemulsion templating dopamine polymerization. The Brunauer–Emmett–Teller (BET) analysis revealed a high surface area of 29.3 m² g⁻¹ and an average pore diameter of  $\approx 20.8$  nm, which are favorable for catalytic loading and substrates diffusion (Figure S2, Supporting Information). Cu, the catalytic core of natural SOD enzymes, was incorporated into mPDA through chelation coordination with catechol moieties during mPDA synthesis. mPDA-Cu presented

a relatively larger hydrodynamic size of 140.6  $\pm$  9.5 nm and a zeta potential of  $-7.8 \pm 1.4$  mV. Selenodimethanamine, the GPx mimic, was incorporated to construct mPDA-Cu/Se via Schiff base reaction or Michael addition.[34] Post-functionalization did not alter the hydrodynamic size and zeta potential of mPDA-Cu (Figure \$3, Supporting Information). X-ray photoelectron spectroscopy (XPS) analysis revealed that Cu and Se within mPDA-Cu/Se closely mimic the active sites of natural SOD and GPx enzymes (Figure \$4, Supporting Information),[35,36] supporting the rational biomimetic design of our cascade nanozyme. Transmission electron microscopy (TEM) revealed well-preserved mesoporous structures (Figure 1a). In addition, elemental mapping confirmed the homogeneous dispersion of Cu and Se elements throughout the nanoparticles with their mass ratios of  $\approx 10.9\%$  and 6.5%, respectively (Figure 1b,c). These mass ratios closely align with the quantitative concentrations determined by inductively coupled plasma mass spectrometry (ICP-MS) (Figure S5, Supporting Information), collectively demonstrating the successful fabrication of mPDA-Cu/Se nanozymes.

To facilitate biocompatible and BBB transverse, mPDA-Cu/Se was further modified with RBCm and BBB-penetrating RVG29 peptide. RVG29, a 29-amino acid peptide derived from rabies virus glycoprotein (RVG), specifically binds nicotinic acetylcholine receptors (nAChRs) overexpressed on brain endothelial cells, enabling receptor-mediated transcytosis across the intact BBB.<sup>[37]</sup> For RVG29 conjugation, DSPE-PEG<sub>2000</sub>-Mal served as an amphiphilic linker: its hydrophobic distearoylphosphatidylethanolamine (DSPE) domain inserted into RBCm bilayer via hydrophobic interactions, while the maleimide group was covalently conjugated to the thiol group of RVG29.[38] Successful synthesis of DSPE-PEG<sub>2000</sub>-RVG29 was verified by <sup>1</sup>Hnuclear magnetic resonance (1H-NMR) spectroscopy, displaying characteristic PEG<sub>2000</sub> ethylene glycol signals ( $\delta$  3.2–3.7 ppm) and RVG29 alkyl proton resonances ( $\delta$  1.4–2.6 ppm) (Figure S6, Supporting Information). RBCm was then functionalized with DSPE-PEG<sub>2000</sub>-RVG29 through simple mixing, followed by co-extrusion with mPDA-Cu/Se at a 1:10 mass ratio to obtain T-mPDA-Cu/Se. The membrane coating process exploited both the robust adhesion properties of catechol groups and electrostatic interactions between the negatively charged membrane surface and amine groups in polydopamine.

TEM imaging confirmed that T-mPDA-Cu/Se was uniformly spherical, showing erythrocyte membrane encapsulation with ≈20 nm thickness on mPDA-Cu/Se surfaces (Figure S7, Supporting Information). T-mPDA-Cu/Se showed a narrow hydrodynamic size distribution (198.2  $\pm$  3.2 nm) and negative zeta potential ( $-17.5 \pm 1.2 \text{ mV}$ ). Sodium dodecyl sulfate-polyacrylamide gel electrophoresis (SDS-PAGE) analysis verified preserved mRBC protein profiles in T-mPDA-Cu/Se (Figure S8, Supporting Information). After two-days of storage in PBS or plasma at 4 °C, TmPDA-Cu/Se revealed negligible variations in particle size, highlighting the colloidal stability for in vivo application (Figure 1f). To assess long-term biosafety, degradation of T-mPDA-Cu/Se was evaluated in a simulated oxidative environment (10 mM H<sub>2</sub>O<sub>2</sub>). Progressive degradation was observed after four days of incubation, indicating favorable metabolic clearance (Figure S9, Supporting Information).

16163028, 0, Downloaded from https://advanced.onlinelibrary.wiley.com/doi/10.1002/adfm.202520000 by Hangzhou Normal University, Wiley Online Library on [10/11/2025]. See the Terms and Conditions (https://onlinelibrary.wiley

and-conditions) on Wiley Online Library for rules of use; OA articles are governed by the applicable Creative Commons License

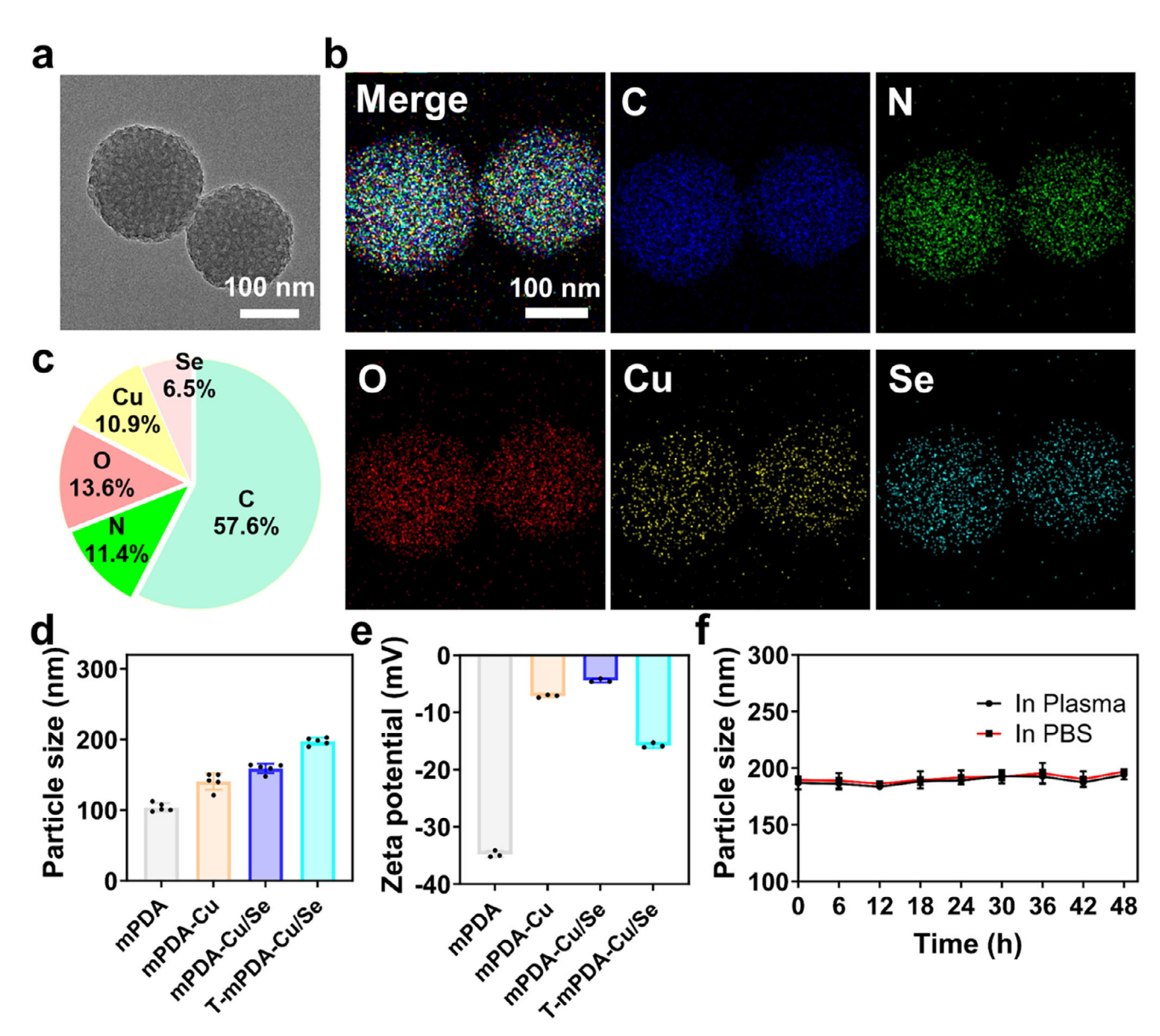


Figure 1. Construction and characterization of T-mPDA-Cu/Se. a) HR-TEM and b) corresponding energy dispersive X-ray elemental mappings of mPDA-Cu/Se, C (blue), N (green), O (red), Cu (yellow), and Se (cyan). c) Mass ratio analyses of mPDA-Cu/Se obtained by elemental mappings. d) Hydrodynamic particle sizes of mPDA, mPDA-Cu/Se, and T-mPDA-Cu/Se. e) Zeta potential values of mPDA, mPDA-Cu/Se, and T-mPDA-Cu/Se (n = 3). f) Colloidal stability of T-mPDA-Cu/Se in PBS and plasma over two days.

### 2.2. SOD-GPx-Mimicking Cascade Activity of mPDA-Cu/Se

CIRI triggers a burst of ROS, driving lipid peroxidation, mitochondrial dysfunction, and DNA damage. Timely ROS neutralization during the acute phase is critical for restoring redox homeostasis and improving neurological outcomes. [39-41] The SOD-GPx-mimicking cascade of mPDA-Cu/Se catalyzes the dismutation of O<sub>2</sub>•- to O<sub>2</sub> and H<sub>2</sub>O<sub>2</sub>, with subsequent conversion to H<sub>2</sub>O by GPx. SOD-mimetic activity was evaluated via a WST-8 assay, where xanthine/xanthine oxidasegenerated O<sub>2</sub>•- reacts with WST-8 to form a water-soluble formazan. [42] mPDA-Cu/Se suppressed formazan formation in a concentration-dependent manner (Figure 2a,b), with an IC<sub>50</sub>

of 250  $\mu g$  mL<sup>-1</sup>. This enhanced catalytic efficiency is attributed to the doped Cu active sites, which lower the activation energy barrier for  $O_2^{\bullet-}$  dismutation, closely mimicking natural SOD activity.<sup>[43]</sup>

Natural GPx leverages the Se-containing active sites to reduce  $\rm H_2O_2$  via the glutathione (GSH)-mediated redox cycle. During the assay,  $\rm H_2O_2$  oxidizes GSH to oxidized glutathione (GSSG), while unreacted GSH reacts with 5,5'-dithiobis-(2-nitrobenzoic acid) (DTNB) to form 5-thio-2-nitrobenzoic acid anion (TNB). GPx-like activity was quantified by monitoring TNB decay kinetics. As shown in Figure 2c, mPDA-Cu/Se exhibited concentration-dependent GSH depletion, achieving maximal activity at 1.0 mg mL $^{-1}$  (Figure S10, Supporting Information).

16163028, 0, Downloaded from https://advanced

onlinelibrary.wiley.com/doi/10.1002/adfm.202520000 by Hangzhou Normal University, Wiley Online Library on [10/11/2025]. See the Terms and Conditions (https://onlinelibrary.wiley.com/term

and-conditions) on Wiley Online Library for rules of use; OA articles are governed by the applicable Creative Commons

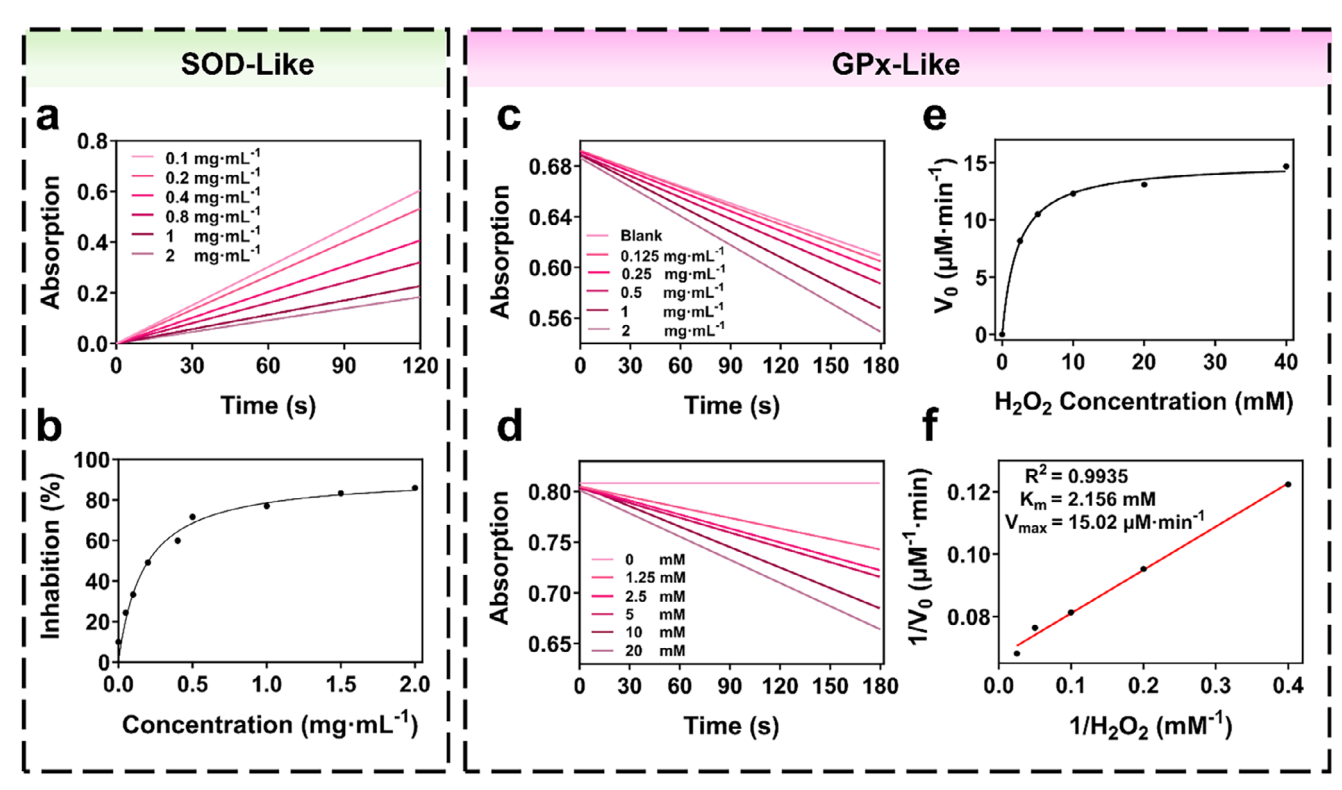


Figure 2. Dual-enzymatic activities and kinetics of mPDA-Cu/Se nanozyme. SOD-like activity: a) Time-dependent absorbance changes of formazan dyes at different concentrations of mPDA-Cu/Se and b) Percentage of inhibition of WST-8 oxidation by O<sub>2</sub> • - vs different concentrations of mPDA-Cu/Se. GPxlike activity: c) Time-dependent absorbance changes of TNB at different concentrations of mPDA-Cu/Se. d) Time-dependent absorbance changes of TNB at different concentrations of  $H_2O_2$ . e) Reaction rates at different concentrations of  $H_2O_2$  and f) Lineweaver-Burk plots of GPx activity corresponding to the variation of GSH concentration.

Steady-state kinetics under varying H2O2 concentrations (Figure 2d,e) revealed classical Michaelis-Menten behavior. Linear Lineweaver-Burk analysis determined a Michaelis constant  $K_m$  of 2.156 mM and a maximum velocity of 15.02  $\mu$ M min<sup>-1</sup> (Figure 2f). Saturation kinetics further confirmed proportionality between nanozyme activity (0-20 mM H<sub>2</sub>O<sub>2</sub>) and catalytic efficiency, validating its enzymatic fidelity. Overall, the Cu/Se-integrated cascade nanozyme boosts ROS clearance via sequential SOD- and GPx-mimicking activities, thereby strengthening synergistic antioxidant defense beyond single component enzyme mimics (Figure S11, Supporting Information).

### 2.3. In Vitro Toxicity of T-mPDA-Cu/Se

The aforementioned investigations have elucidated the cascaded enzyme mimetic capabilities of the mPDA-Cu/Se nanozyme, demonstrating its robust antioxidant potential. Subsequently, the viability of T-mPDA-Cu/Se was evaluated in PC12 (rat adrenal medulla-derived neural model) and bEnd.3 (murine brain endothelial) cell lines to simulate central nervous system and brain endothelial cells by the CCK-8 assay.[44] Over 90% cells were viable after incubation with T-mPDA-Cu/Se at a concentration of 80.0 µg mL<sup>-1</sup> for 16 h in both cell lines (Figure S12, Supporting Information). Calcein-AM/PI dual staining also confirmed minimal acute toxicity of T-mPDA-Cu/Se in both cell lines, as most cells exhibited green fluorescence (viable cells) at the same incubation conditions (Figure 3a). Flow cytometry quantification via Annexin V-FITC/PI double staining showed 98.5% of PC12 cells and 90.6% of bEnd.3 cells were Annexin V-FITC-/PI-, without noticeable cell apoptosis (Figure 3b). To investigate cellular uptake characteristics, we performed cellular uptake experiments on bEnd.3 and PC12 cells using Cy5-labeled T-mPDA-Cu/Se. Confocal laser scanning microscopy (CLSM) images revealed a time-dependent increase in uptake by both cell types (Figures \$13 and \$14, Supporting Information). To further assess cellular biosafety, we investigated T-mPDA-Cu/Se nanozyme degradation in PC-12 cells using Bio-TEM. Following 3-day incubation, nanozyme debris was observed in lysosomes, with obvious size reduction corroborating degradation (Figure \$15, Supporting Information). These results collectively demonstrate the system's excellent biocompatibility and suitability for subsequent applications.

### 2.4. In Vitro Neuronal Cells Protection of T-mPDA-Cu/Se

Building on confirmed ROS scavenging efficacy and biocompatibility of T-mPDA-Cu/Se, we evaluated its antioxidant performance in an in vitro ischemic stroke OGD/R model.[45] Figure 4a illustrates the experimental timeline where nanozymes were administered after 4 h hypoxia exposure, followed by 12 h reoxygenation. Intracellular ROS levels were quantified using

16163028, 0, Downloaded from https://advanced.onlinelibrary.wiley.com/doi/10.1002/adfm.202520000 by Hangzhou Normal University, Wiley Online Library on [10/11/2025]. See the Terms

conditions) on Wiley Online Library for rules of use; OA articles are governed by the applicable Creative Commons

www.afm-journal.de

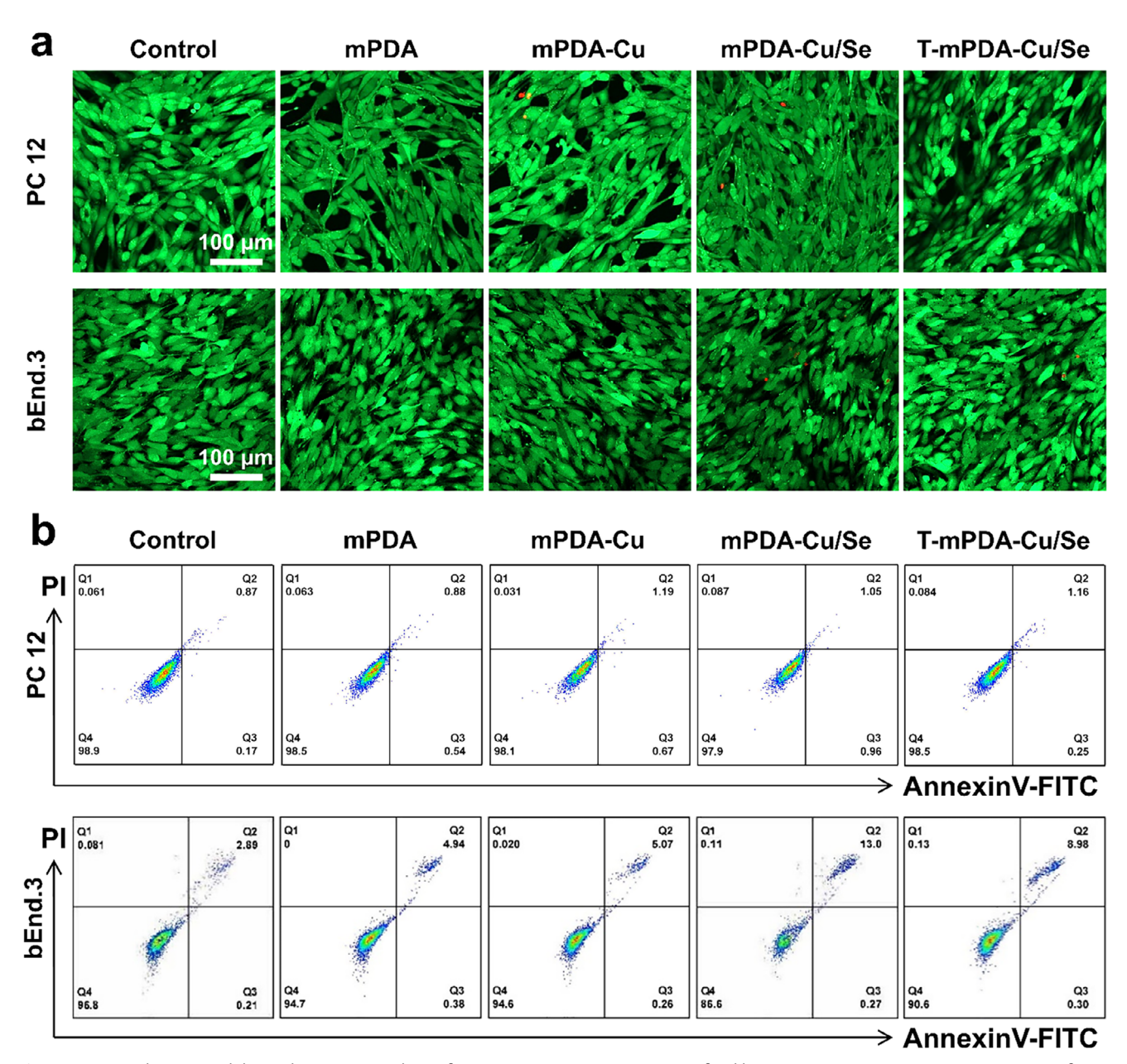


Figure 3. In vitro biocompatibility and apoptosis analysis of T-mPDA-Cu/Se nanozyme. a) Confocal laser scanning microscopy (CLSM) images of PC12 and bEnd.3 cells co-stained with Calcein AM (green, live) and PI (red, dead). b) Flow cytometry apoptosis profiles via Annexin V-FITC/PI dual staining.

2,7-dichlorodi-hydrofluorescein diacetate (DCFH-DA) fluorescence at a nanozyme concentration of 20.0  $\mu$ g mL<sup>-1</sup>. Flow cytometry analysis displayed that OGD/R-treated cells exhibited significantly elevated intracellular ROS levels vs control (Figure 4b). [46] All nanoparticles exhibited ROS attenuation capacity, with efficacy ranking as T-mPDA-Cu/Se (75.8%)  $\approx$  mPDA-Cu/Se (74.4%) > mPDA-Cu (63.2%) > mPDA (23.1%). Confocal imaging also verified that T-mPDA-Cu/Se nearly abolished OGD/R-induced ROS in PC12 cells (Figure 4c,e). Consistent results were observed in mitochondrial ROS levels, as quantified via Mito-SOX fluorescence (Figure 4d,f).

Excessive ROS induces mitochondrial membrane oxidative damage, disrupting mitochondrial membrane potential

(MMP).<sup>[47]</sup> Loss of MMP triggers mitochondrial permeability increase, cytochrome c release into the cytosol, and subsequent apoptotic cascade activation. JC-1 probe was used to evaluate the MMP changes in PC12 cells subjected to OGD/R: healthy mitochondria maintained red-fluorescent Jaggregates of JC-1, while MMP loss shifts emission to green monomers. OGD/R treatment increased the JC-1 red-to-green intensity ratio, indicating that mitochondrial damage was relieved (Figure 4g,h).

To validate in vitro BBB permeability, a transwell co-culture system with bEnd.3 cells (upper chamber) and PC12 cells (basal chamber) were employed (Figure 4i).  $100.0~\mu g~mL^{-1}$  of FITC-labeled nanozymes were introduced into the upper chamber,

16163028, 0, Downloaded from https://advanced.

onlinelibrary.wiley.com/doi/10.1002/adfm.202520000 by Hangzhou Normal University, Wiley Online Library on [10/11/2025]. See the Terms and Conditions (https://onlinelibrary.wiley.

onditions) on Wiley Online Library for rules of use; OA articles are governed by the applicable Creative Commons License

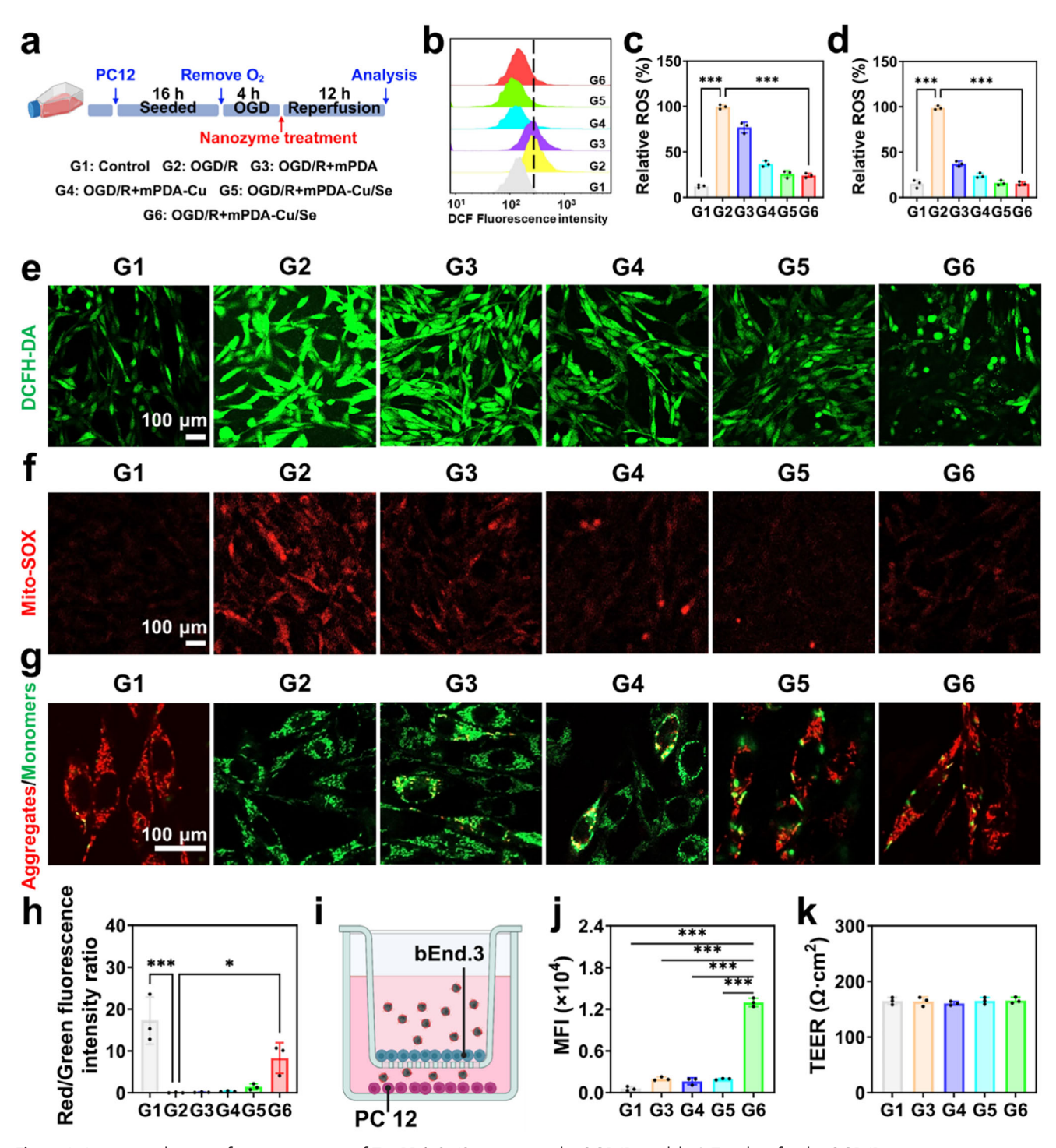


Figure 4. In vitro evaluation of neuroprotection of T-mPDA-Cu/Se nanozyme by OGD/R model. a) Timeline for the OGD/R experiments to investigate the therapeutic effect of T-mPDA-Cu/Se nanozyme. b) The mean DCF fluorescence intensity was monitored with flow cytometry. c) Quantitative analysis of DCF fluorescence intensity. d) Histogram illustrating the quantitative analysis of Mito-SOX fluorescence intensity. e) Typical CLSM images of the DCF fluorescence of Control, OGD/R, OGD/R+mPDA, OGD/R+mPDA-Cu, OGD/R+mPDA-Cu/Se, and OGD/R+T-mPDA-Cu/Se groups with nanozyme concentrations at 20  $\mu$ g mL<sup>-1</sup>. f) Typical CLSM images of mitochondria labeled with the Mito-SOX fluorescent probe across treatment groups. g) Representative CLSM images of PC12 cells labeled with JC-1 fluorescent probe across treatment groups. h) Quantified percentage of JC-1 aggregates in PC12 cells across treatment groups. i) Schematic illustration of the transwell model used for evaluating nanoparticle transport. j) Quantitative analysis of the transport efficiency in the transwell model. k) Validation of endothelial barrier integrity via TEER measurement. Statistical analysis was performed using a one-way ANOVA test followed by Tukey's multiple comparison analysis. n = 3, p < 0.05, p < 0.01, and p < 0.001.

16163028, 0, Downloaded from https://advanced.onlinelibrary.wiley.com/doi/10.1002/adfm202520000 by Hangzhou Normal University, Wiley Online Library on [10/11/2025]. See the Terms and Conditions (https://onlinelibrary.wiley.com/terms/

and-conditions) on Wiley Online Library for rules of use; OA articles are governed by the applicable Creative Commons License

www.afm-journal.de

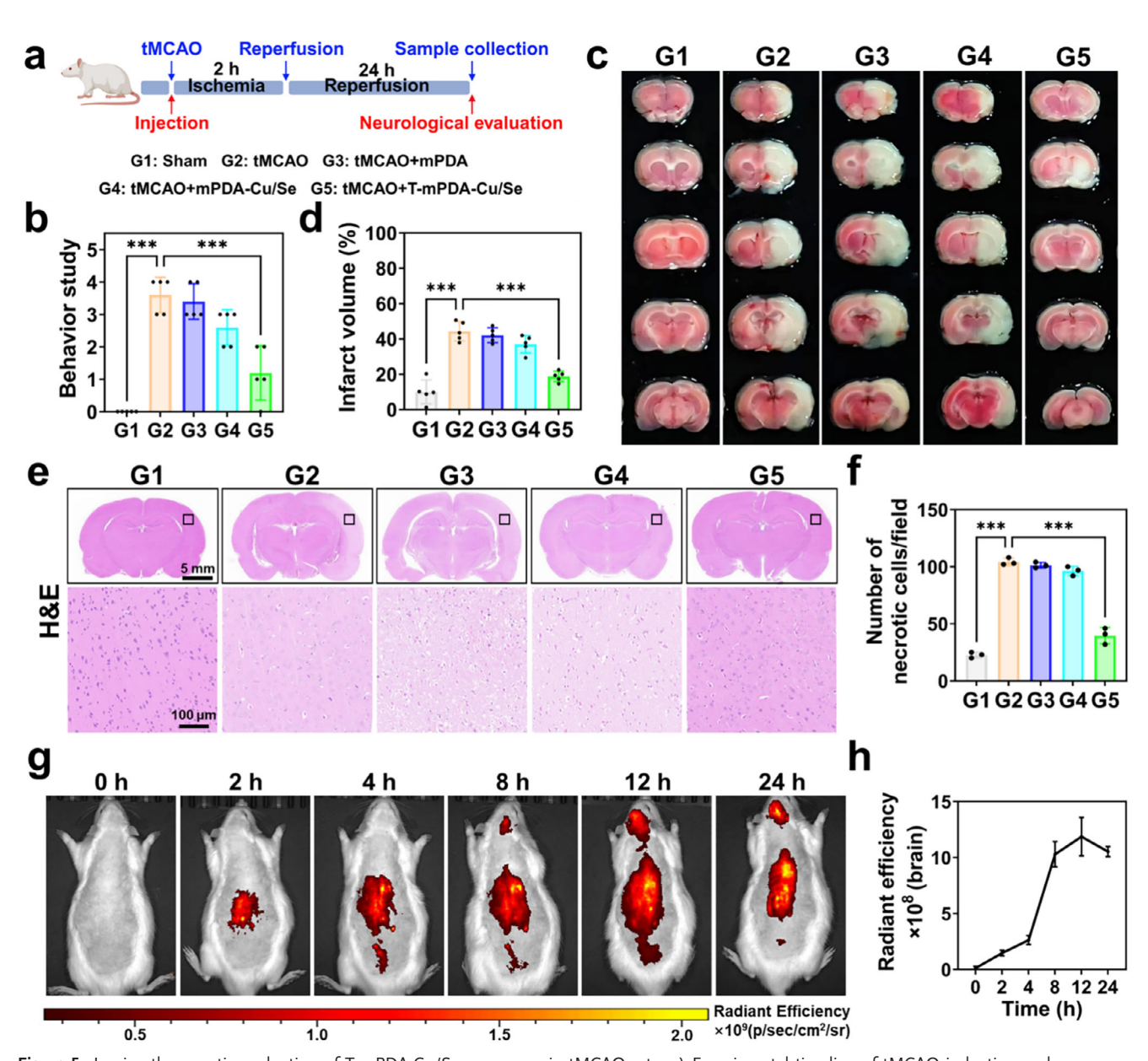


Figure 5. In vivo therapeutic evaluation of T-mPDA-Cu/Se nanozyme in tMCAO rats. a) Experimental timeline of tMCAO induction and nanozyme administration. b) Neurological deficit evaluation by Longa score behavioral tests (n = 5). c) Representative images of TTC-stained brain sections with ischemic regions in grayish-white and viable tissue in red. d) Quantified cerebral infarct volume of tMCAO rats in each treatment group at 24 h post-stroke (n = 5). e) Representative H&E staining images of brain tissue and f) quantitative assessment of necrotic cell counts in each group (n = 3). g) In vivo fluorescence imaging of tMCAO mice treated with Cy5.5-labeled T-mPDA-Cu/Se and h) corresponding time-radiant efficiency analysis of the brain regions (n = 3). Statistical analysis used a one-way ANOVA test followed by Tukey's multiple comparison analysis. \*p < 0.05, \*\*p < 0.01, and \*\*\*p < 0.001.

and transendothelial transport efficiency was quantified by measuring fluorescence of cell culture medium in the basal chamber after 2 h incubation. Figure 4j shows that T-mPDA-Cu/Se achieved six- to eight-fold higher transport efficiency vs other groups, confirming RVG29-mediated BBB penetration efficacy. This enhanced permeability did not damage endothelial integrity, as TEER measurements remained stable (>150  $\Omega$  cm²) across all groups (Figure 4k).

### 2.5. In Vivo Therapeutic Effects of T-mPDA-Cu/Se

The in vivo therapeutic effects were systematically evaluated using a tMCAO model. As illustrated in **Figure 5a**, tMCAO model was established in Sprague–Dawley (SD) rats by inserting a silicone-coated nylon suture into the middle cerebral artery for 2 h, followed by suture withdrawal and surgical closure to initiate reperfusion.<sup>[17]</sup> Nanozyme administration via tail vein

1616328, D. Downloaded from https://advanced.onlinelibrary.wiley.com/doi/10.1002adfm.202520000 by Haggzbou Normal University, Wiley Online Library on [10/11/205]. See the Terms and Conditions (https://onlinelibrary.wiley.com/terms-and-conditions) on Wiley Online Library for rules of use; OA articles are governed by the applicable Creative Commons License

injection was synchronized with arterial occlusion to ensure precise therapeutic intervention timing. Neurological deficits were quantitatively assessed 24 h post-surgery using the Longa scoring method.[48] Rats treated with T-mPDA-Cu/Se exhibited significantly lower Longa scores compared to tMCAO controls, approaching levels observed in sham-operated animals as shown in Figure 5b. To further characterize motor function recovery, a beam walking test revealed that tMCAO rats experienced slipping off the beam for 3-5 times due to impaired coordination, whereas T-mPDA-Cu/Se treated rats demonstrated near-normal motor performance with only ≈1 slip (Figure S16, Supporting Information).[49] Complementary behavioral analysis using the adhesive removal test showed that tMCAO rats required ≈120 s to detach tape from their affected forepaw, while the T-mPDA-Cu/Se treatment reduced this latency to ≈45 s, confirming attenuated neurological deficits and enhanced sensorimotor recovery (Figure S17, Supporting Information).[50]

2,3,5-Triphenyltetrazolium chloride (TTC) staining validated the neuroprotective efficacy of T-mPDA-Cu/Se, with ischemic regions (grayish-white) in tMCAO rats contrasting sharply against the red formazan signal in viable tissues (Figure 5c).[51] Treatment with T-mPDA-Cu/Se reduced the cerebral infarct volume from 44.3  $\pm$  6.4% (untreated tMCAO group) to 18.8  $\pm$  3.7% (Figure 5d), due to its dual capacity to traverse the BBB and ameliorate ischemia-reperfusion induced ROS surges. Histopathological analysis conducted via hematoxylin-eosin (HE) staining further corroborated the neuroprotective effects (Figure 5e). T-mPDA-Cu/Se treatment significantly reduced the number of necrotic cells (39.7 ± 6.3 cells) showing nuclear pyknosis characteristics in the cerebral ischemic region, compared with the tMCAO group (104.3  $\pm$  3.5 cells) (Figure 5f). Additionally, comprehensive safety assessments further validated the translational potential of T-mPDA-Cu/Se nanozyme system. No hemolysis was observed at the therapeutic concentration of 200 µg mL<sup>-1</sup> (Figure S18, Supporting Information), and blood biochemical parameters, including alanine aminotransferase (ALT) and aspartate aminotransferase (AST) remained within physiological ranges (Figure S19, Supporting Information). Microscopic examination of major organ tissues of mice, including heart, liver, spleen, lungs, and kidney, revealed no obvious pathological alterations (Figure S20, Supporting Information), underscoring the systemic biosafety of T-mPDA-Cu/Se.

To evaluate the brain-targeted delivery, Cyanine 5.5-labeled T-mPDA-Cu/Se were tracked via in vivo imaging. As demonstrated in Figure 5g,h, post-injection fluorescence imaging revealed maximal intensity in ischemic brains at 12 h and sustained over 24 h. The brain tissues were excised at 24 h post-injection and observed using the in vivo imaging system. T-mPDA-Cu/Se exhibited a preferential distribution in the ischemic hemispheres compared to the normal hemispheres, which was attributed to the damaged BBB in the ischemic regions (Figure S21, Supporting Information). Crucially, the T-mPDA-Cu/Se nanozyme demonstrated favorable in vivo kinetics with near-complete systemic clearance within 72 h (Figure S22, Supporting Information) while sustaining therapeutic efficacy as evidenced by persistently alleviated neurological deficits (Figure S23, Supporting Information).

## 2.6. Suppression of Neuroinflammation and Neuronal Apoptosis by T-mPDA-Cu/Se Nanozyme

CIRI induces massive glial cell activation in the brain, leading to glial scar formation that impairs endogenous neurorepair. [52] Immunofluorescence staining of penumbra section revealed that glial fibrillary acidic protein (GFAP, a mature astrocyte marker) expression was upregulated to 15.4 ± 1.1% of total cells in tM-CAO mice, which was significantly attenuated to 1.4  $\pm$  0.2% following T-mPDA-Cu/Se treatment (Figure 6a,b). Microglial polarization analysis demonstrated dramatically reduced CD86+ cells (pro-inflammatory phenotype) and increased CD206+ cells (antiinflammatory phenotype) in T-mPDA-Cu/Se-treated mice compared to tMCAO controls (Figure 6c,d). Quantitative PCR revealed that T-mPDA-Cu/Se significantly decreased mRNA levels of pro-inflammatory cytokine IL-1 $\beta$  (22.4% of tMCAO) and IL-6 (25% of tMCAO), but increased anti-inflammatory IL-4 (3.7-fold) and IL-10 (4.8-fold) expression (Figure 6e-h). We further quantified cerebral necrosis by using the terminal deoxynucleotidyl transferase dUTP nick-end labeling (TUNEL) assay, a well-established method for detecting DNA fragmentation via green fluorescence labeling. tMCAO group exhibited extensive apoptotic signaling, with 89.9 ± 1.6% of cells displaying fluorescence (Figure 6i,i). Remarkably, T-mPDA-Cu/Se treatment reduced apoptotic cell ratios to 15.8 ± 1.7%, underscoring its capacity to mitigate cell death. These findings, combined with earlier evidence of inflammatory modulation (reduced GFAP/CD86/IL- $1\beta/IL$ -6 levels, and elevated CD206/IL-4/IL-10 levels), confirm that T-mPDA-Cu/Se efficiently inhibits inflammation and apoptosis, exerting comprehensive neuroprotection against CIRI.

### 3. Conclusion

In summary, this study presents a biomimetic T-mPDA-Cu/Se nanozyme system engineered to combat CIRI through mitigating oxidative stress and neuroinflammation. By integrating Cu and Se into mPDA scaffolds, T-mPDA-Cu/Se exhibits cascade SOD-GPx-like enzymatic activities, while functionalization with BBB-targeting RVG29 peptide and RBCm coating enhances BBB trans and biocompatibility. T-mPDA-Cu/Se mitigated OGD/Rinduced neuronal apoptosis via potent ROS scavenging in vitro. In tMCAO rat models, T-mPDA-Cu/Se efficiently reduced cerebral infarct volume from 44.3% to 18.8%, suppressed apoptosis from 89.9% to 15.8%, and significantly improved neurological recovery. Mechanistically, it inhibited astrocyte activation and microglial pro-inflammatory polarization, modulating cytokine expression from pro-(IL-1 $\beta$ /IL-6) to anti-inflammatory (IL-4/IL-10) profiles. Systemic biosafety evaluations confirmed no hepatorenal toxicity or histopathological anomalies, underscoring its high biosafety. By synergistically targeting oxidative stress and neuroinflammation without exogenous drugs, this work advances nanomaterial innovation for clinical neuroprotection, offering a promising approach to ischemic stroke therapy.

## 4. Experimental Section

Materials: Pluronic F127 (9003-11-6), dopamine hydrochloride (62-31-7), 1,3,5-trimethylbenzene (108-67-8), copper sulfate pentahydrate

16163028, 0, Downloaded from https://advanced.onlinelibrary.wiley.com/doi/10.1002/adfm.202520000 by Hangzhou Normal University, Wiley Online Library on [10/11/2025]. See the Terms

and Conditions (https://onlinelibrary.wiley.com/ten

-conditions) on Wiley Online Library for rules of use; OA articles are governed by the applicable Creative Commons

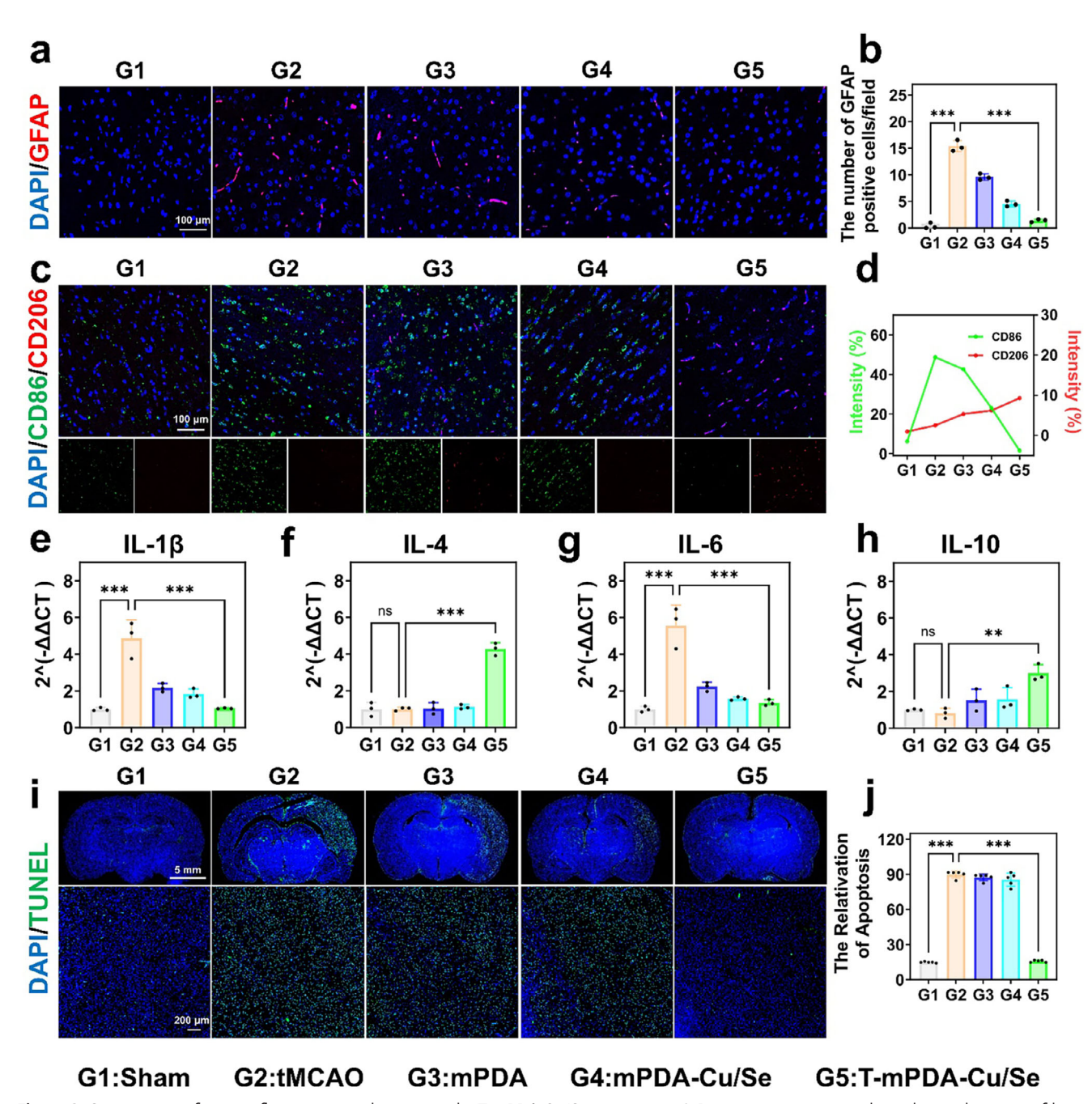


Figure 6. Suppression of neuroinflammation and apoptosis by T-mPDA-Cu/Se nanozyme. a) Representative immunohistochemical images of brain tissue stained with GFAP antibody. b) Quantitative analyses of the number of GFAP-positive cells in the penumbral regions in each treatment group at 24 h post-stroke (n = 3). c) Representative immunofluorescent images stained with CD86 and CD206 antibodies and d) quantitative analyses of the fluorescent intensity. Relative mRNA transcription of e) IL-1 $\beta$ , f) IL-6, g) IL-4, and h) IL-10 in brain tissue from different groups confirmed by qPCR (n = 3). i) Representative TUNEL staining images of brain tissue from different groups and j) Quantitative analysis of the apoptosis index in the penumbral regions (n = 5). Statistical analysis used a one-way ANOVA test followed by Tukey's multiple comparison analysis. \*p < 0.05, \*\*p < 0.01, and \*\*\*p < 0.001.

(7758-99-8), ammonia solution (1336-21-6), DSPE-PEG<sub>2000</sub>-MAL (474922-22-0) were purchased from Sigma-Aldrich (St. Louis, MO, USA). CD 86 antibody (ab238468) and CD 206 antibody (ab300621) were obtained from abcam (Cambridge, CB, UK). Cell Counting Kit-8 (CCK-8, MA 0218), fluorescein isothiocyanate (FITC, MA0220), 2',7'-dichlorodihydrofluorescein diacetate (DCFH-DA, MB4682), and JC-1 (MA0338\_A) were procured

from Dalian Meilun Biotechnology Co., Ltd. (Dalian, China). 2,3,5-Triphenyltetrazolium chloride (TTC, G3005) was provided by Beijing Solarbio Science & Technology Co., Ltd. (Beijing, China). Mitochondrial ROS fluorescence probe (Mito-SOX Red, HY-D1055), Calcein-AM (HY-D0041) and RVG29 (115136-25-9) were purchased from Med Chem Express Biotech Co., Ltd. (Shanghai, China). GFAP antibody (GB 11096) was

16163028. 0, Downloaded from https://advanced.onlinelibrary.wiley.com/doi/10.1002/adfm.202520000 by Hangzhou Normal University, Wiley Online Library on [10/11/2025]. See the Terms

and Conditions (https://onlinelibrary.wiley.com/term

and-conditions) on Wiley Online Library for rules of use; OA articles are governed by the applicable Creative Commons

obtained from Servicebio (Wuhan, China). All animal experimental instruments were purchased from Shenzhen Ruiwode Life Technology Co., Ltd. (Shenzhen, China).

Cells: Murine brain microvascular endothelial cells (bEnd.3 cells), and rat neuronal PC12 cells were obtained from Servicebio (Wuhan, China). bEnd.3 cells and PC12 cells were cultured in Roswell Park Memorial Institute 1640 medium containing 10% FBS (fetal bovine serum, Biosharp) and 1% PS (penicillin-streptomycin, Meilunbio) at 37 °C in an incubator with 5% CO<sub>2</sub>.

Animals: Male SD rats were purchased from Shanghai Jihui Laboratory Animal Care Co., Ltd. (Shanghai, China). All animal experiments were approved by the Animal Experiment Ethics Review Committee of Hangzhou Normal University (Approval No. HSD-20240108-02) and the "Guidelines for the Care and Use of Laboratory Animals" of the Chinese Academy of Sciences.

Preparation of mPDA-Cu/Se NPs: The synthesis of mPDA nanoparticles commenced with a well-established protocol. F127 (15 mg) and dopamine (100 mg) were ultrasonically dispersed in a 50% ethanolic solution (50 mL). To this mixture, 600 µL of 1,3,5-trimethylbenzene was introduced into the flask. The solution was sonicated for 3 min and then subjected to stirring for 1 h, after which 6 mg of copper sulfate pentahydrate was incorporated, and the stirring continued for 1 h, resulting in a color transition from white to pink. Subsequently, 300 µL of ammonia solution was introduced to catalyze the reaction. The crude nanoparticles were harvested by centrifugation (×10 000 g, 10 min). The removal of 1,3,5-trimethylbenzene and F127 polymer was achieved through ethanolic reflux, yielding purified mPDA-Cu NPs. These nanoparticles underwent lyophilization and were conserved at 4 °C for subsequent utilization. For the fabrication of mPDA-Cu/Se NPs, 10 mg of mPDA-Cu NPs were dispersed in PBS at pH 8.5, to which 1 mg of selenodimethionine was added, and the mixture was stirred for 3 h. The resulting mPDA-Cu/Se NPs were lyophilized and stored at 4 °C for future applications. The structural and morphological characteristics of mPDA, mPDA-Cu NPs, and mPDA-Cu/Se NPs were examined using TEM and elemental mapping.

RBCm Extraction: RBCm were extracted from male SD rat blood using a differential centrifugation method. The detailed procedure was as follows: A 200 g rat was an esthetized with 2.5 mL of 1% pentobarbital sodium. The abdominal cavity was then opened to collect whole blood from the abdominal aorta, which was placed into a 10 mL centrifuge tube containing of EDTA-2Na anticoagulant solution. After centrifugation at 4 °C (×100 g, 20 min), the supernatant was discarded, and the pellet was resuspended in 1x PBS and allowed to stand in an ice bath for 10 min. Following another centrifugation to remove the supernatant, five volumes of 0.25× PBS were added, and the mixture was gently inverted in the ice bath every ten minutes. After a 2 h incubation, the mixture was centrifuged (4 °C, ×100 g, 10 min), the supernatant was discarded, and the pellet was washed with 0.25× PBS until the supernatant remained colorless. The isolated RBCm were stored in 1× PBS, presenting as a transparent, flocculent

Synthesis of the T- mPDA-Cu/Se Nanozyme: 2 mg of RVG29 powder and 5 mg of DSPE-PEG<sub>2000</sub>-MAL were dissolved in 5 mL of anhydrous DMF (N, N-dimethylformamide) and stirred at room temperature for 24 h. The reaction solution was then transferred into a dialysis bag (cutoff molecular weight of 1000 Da), and after dialysis against pure water for 24 h, the product was freeze-dried to obtain DSPE-PEG<sub>2000</sub>-RVG29, which was characterized using  $^1H$ -NMR spectroscopy. To prepare T-RBCm,  $800\,\mu L$  of RBCm dispersion (extracted from 1 mL of whole blood) was added to 3 mL of PBS containing DSPE-PEG  $_{\rm 2000}\text{-RVG29}$  (1 mg  $\rm mL^{-1})$  . The mixture was incubated at 37 °C for 24 h. After washing via centrifugation, the purified T-RBCm was then incubated with 10 mg of mPDA-Cu/Se NPs at 37 °C and co-extruded using a hand extruder to yield the T- mPDA-Cu/Se nanozyme. The loading of RBCm and RVG29 was characterized by sodium dodecyl sulfate-polyacrylamide gel electrophoresis (SDS-PAGE). The morphology and structure of the T-mPDA-Cu/Se nanozyme were observed using TEM. The stability of the T- mPDA-Cu/Se nanozyme was monitored by measuring the size fluctuations in PBS and plasma over two days.

SOD-Like Activity of mPDA, mPDA-Cu, mPDA-Cu/Se, and T-mPDA-Cu/Se: The SOD-like activity was assessed utilizing a Total SODActivity Assay Kit (WST-8, BL903A). WST-8 interacts with O2 •-, which are generated by the catalytic reaction of xanthine oxidase, to produce water-soluble formazan dyes. Given that SOD facilitates the dismutation of superoxide anions, SOD activity is inversely proportional to the formazan dye formation. The SOD-like activity was quantified by monitoring the oxidation of WST-8 at 450 nm to form orange-yellow formazan, using a UV-vis spectrophotometer.

GPx-Like Activity of mPDA, mPDA-Cu, mPDA-Cu/Se, and T-mPDA-Cu/Se: GPx activity was determined by its ability to catalyze the reaction between reduced glutathione (GSH) and hydrogen peroxide (H2O2), resulting in the formation of oxidized glutathione (GSSG). The reaction of GSH with 5,5'-dithiobis-(2-nitrobenzoic acid) (DTNB) yields a yellow colored 5-thio-2-nitrobenzoic acid anion (TNB). The GPx activity was calculated by measuring the change in the maximum absorption peak of TNB at 412 nm. The reaction was conducted at 37  $^{\circ}$ C in a 500  $\mu$ L solution containing PBS (pH 7.4, 1.0 mM EDTA), 1.0 mM GSH, and various concentrations of the nanozyme dissolved in PBS. After a 3 min incubation at 37 °C, 0.25 mM DTNB solution was added, followed by a further 1 min incubation. Initiation of the reaction was done by adding 0.5 m-M H<sub>2</sub>O<sub>2</sub>. The activity was ascertained by measuring the decrease in absorbance of TNB at 412 nm using a UV-vis spectrophotometer.

Cell Culture and Cytotoxicity Assessment: For the in vitro evaluation of the nanozyme, the PC12 and bEnd.3 cell lines were aerobically cultured in RPMI-1640 medium enriched with 10% fetal bovine serum (FBS) and 1% penicillin-streptomycin (PS) solution, under controlled conditions at 37 °C in an atmosphere containing 5% CO2. Cell studies were initiated utilizing cells that were actively proliferating in the logarithmic phase. The biocompatibility assessment was performed employing the CCK-8 assay kit. The cells were inoculated into a 96 well microplate at a seeding density of  $1 \times 10^4$  cells per well. After a 24 h adhesion period, the cells were exposed to a range of concentrations of the preparation (0–80  $\mu$ g mL<sup>-1</sup>) for a 12 h incubation. Subsequently, 10 µL of the CCK-8 reagent was introduced into each well for a further 30 min incubation. The cell viability was determined by quantifying the absorbance at 450 nm using a microplate spectrophotometer.

Oxygen and Glucose Deprivation/Reperfusion (OGD/R) Model: To mimic CIRI in vitro, cells were subjected to an OGD/R regimen. PC12 and bEnd.3 cells were inoculated into culture flasks at optimal densities and permitted to adhere for 24 h. The cells were then rinsed three times with 1× PBS and incubated in glucose free RPMI-1640 medium. The cells were transferred to a hypoxic chamber composed of 95% N<sub>2</sub> and 5% CO<sub>2</sub>, and maintained under glucose and oxygen deprivation conditions at 37 °C for 24 h. Following the OGD period, the medium was replaced with RPMI-1640 medium containing elevated levels of glucose to simulate reperfusion, and the cells were returned to a normoxic incubator for an additional 16 h. To investigate the protective effects of the nanozyme on cellular integrity, cells were treated with PBS, mPDA, mPDA-Cu, mPDA-Cu/Se, and T-mPDA-Cu/Se, respectively.

Live/Dead Cell Fluorescence Assay: Calcein-AM, a membranepermeable dye, was hydrolyzed by esterases within viable cells, resulting in its retention and the emission of intense green fluorescence. In contrast, Propidium Iodide (PI), a membrane-impermeable nucleic acid stain, penetrates compromised cell membranes and binds to DNA, emitting red fluorescence. This Calcein-AM/PI dual-fluorescence staining protocol was utilized to discern cellular viability and mortality, with Calcein-AM staining live cells and PI staining dead cells. Cells were plated in an eight well chambered coverglass at a density of  $1 \times 10^5$  cells per well and allowed to adhere for 16 h. Following incubation under normoxic conditions or exposure to OGD/R stress, the cells were treated according to the experimental groups. Cellular fluorescence was visualized using a confocal laser scanning microscope (CLSM, Zeiss, LSM-900).

Research on Antioxidants in Cells: DCFH-DA can be intracellularly hydrolyzed by esterases into 2',7'-dichlorodihydrofluorescein (DCFH). This compound is subsequently oxidized by ROS within the cell, transforming into 2',7'-dichlorofluorescein (DCF) with a distinctive green fluorescence. Therefore, the DCFH-DA ROS Assay Kit was utilized to detect ROS generation in cells subjected to oxygen-glucose deprivation/reperfusion (OGD/R). The intensity of DCF fluorescence serves as a direct indicator

1616328, D. Downloaded from https://advanced.onlinelibrary.wiley.com/doi/10.1002adfm.202520000 by Haggzbou Normal University, Wiley Online Library on [10/11/205]. See the Terms and Conditions (https://onlinelibrary.wiley.com/terms-and-conditions) on Wiley Online Library for rules of use; OA articles are governed by the applicable Creative Commons License

of the intracellular ROS level. Cells were plated in eight well confocal dishes at a density of  $1\times10^6$  cells per well and allowed to adhere for 24 h. Subsequently, cells from each group were trypsinized, incubated with DCFH-DA (10  $\mu M)$  in the dark at 37 °C for 30 min, centrifuged, gently washed three times with PBS, and resuspended. Intracellular ROS levels in each group were then quantitatively assessed by flow cytometry (BD Bioscience, FACSCelesta) at excitation and emission wavelengths of 488 and 525 nm, respectively.

Assessment of Apoptosis by Flow Cytometry: The Annexin V-fluorescein isothiocyanate (FITC)/propidium iodide (PI) double staining apoptosis detection kit was employed to evaluate cell apoptosis. During early stages of apoptosis, phosphatidylserine (PS) translocates to the outer leaflet of the cell membrane and binds to Annexin V. PI stains cells that have lost membrane integrity during late apoptosis or necrosis. Cells were seeded in six-well plates at a density of  $1\times10^6$  cells per well and allowed to adhere for 16 h. Then the cells from each group were trypsinized, centrifuged, washed with PBS, and centrifuged twice. Following this, the cells were suspended in buffer provided by the kit, stained with 5  $\mu L$  of Annexin V-FITC and 5  $\mu L$  of PI at room temperature for 15 min, centrifuged, washed with PBS, and centrifuged once more. The cell apoptosis status was then evaluated by flow cytometry (BD Bioscience, FACSCelesta) after resuspension in the kit's buffer.

Detection of Mitochondrial Membrane Potential (MMP) After OGD/R Using Fluorescent Probe JC-1: OGD/R can induce mitochondrial dysfunction, characterized by a decrease in membrane potential. JC-1 is a fluorescent probe specifically designed to detect mitochondrial membrane potential. In cells with high mitochondrial membrane potential, JC-1 aggregates in the mitochondrial matrix and emits red fluorescence. Conversely, in cells with low membrane potential, JC-1 remains in the cytoplasm and emits green fluorescence. The transition of JC-1 from red to green fluorescence serves as an early indicator of apoptosis. Cells were plated in eightwell confocal dishes at a density of  $1 \times 10^5$  cells per dish and allowed to adhere for 16 h. After that, the medium was aspirated, and  $300~\mu$ L of JC-1 working solution was added. The cells were then incubated in the dark at 37~C for 20 min. Cellular fluorescence was observed using a confocal laser scanning microscope (CLSM, Zeiss, LSM-900) to assess MMP.

Transwell Model: The in vitro BBB model was established as described. Briefly, both bEnd.3 and PC12 were first cultured in complete media (DMEM with 10% FBS and 1% PS) in a flask at 37 °C in a humidified incubator with 5% CO<sub>2</sub> to reach confluency before being moved to inserts. Next, PC12 were seeded on the bottom of the 24-well plates at a density of 2  $\times$  10  $^{5}$  cells cm  $^{-2}$ . After 24 h of adhesion, bEnd.3 cells were seeded onto the upper side of the collagen-coated Transwell PC membrane inserts with 0.3  $\mu m$  pores at a density of 2  $\times$  10<sup>5</sup> cells cm<sup>-2</sup>, and the inserts were placed in 24-well plates containing PC12. The well plates with inserts were incubated by changing the medium every day in the outer well until cell confluency was reached. It was then considered suitable for BBB transport studies once the TEER values exceeded 150  $\Omega$  cm $^{2}$ , indicating a sufficiently tight monolayer formation. The nanozymes were added to the upper chamber of the models to screen the transport profile. After 2 h of incubation, 800 µL aliquots from the basal chamber were collected, centrifuged, and analyzed via fluorescence spectrophotometry at 695 nm.

Development of a Rodent Model for tMCAO to Emulate CIRI: A highly controlled rat model of transient cerebral ischemia was established through the employment of the suture occlusion methodology. Male Sprague-Dawley rats, weighing precisely between 180 and 200 g, were meticulously chosen and anesthetized. The surgical procedure involved exposing the common carotid artery (CCA), followed by the careful isolation of the external carotid artery (ECA) and internal carotid artery (ICA). The CCA was then ligated, and the ECA was clamped with an artery clip to facilitate the insertion of a customized silicone-coated nylon suture from the CCA into the ICA, thereby occluding blood flow in the middle cerebral artery. The ECA was released simultaneously. After maintaining the occlusion for a duration of 1.5 h, the nylon suture was gently retrieved initiate reperfusion. To maintain normothermic conditions throughout the surgical procedure, a heating pad was utilized. The nanozymes were intravenously administered via tail vein injection at a dose of 5 mg k<sup>-1</sup>g body weight.

Neurobehavioral Evaluation Post-tMCAO Surgery: A comprehensive neurobehavioral assessment was conducted on the rats 24 h after surgery, utilizing a standardized neurological deficit score. The scoring system was as follows: a score of 0 indicated no deficit, 1 = flexion of the forepaw, 2 = circling to the contralateral side, 3 = falling to one side during locomotion, 4 = the absence of spontaneous movement, and 5 = death. Rats that scored between 1 and 3 were deemed to have undergone successful surgery and were eligible for subsequent experimental procedures.

Beam Walking Test: A 1 m long, 1.5 cm wide beam platform was constructed. Three days prior to tMCAO surgery, animals were trained to traverse the beam until achieving fully autonomous locomotion, with traversal time and number of foot slips recorded. At 24 h post-tMCAO surgery, beam traversal performance was re-evaluated, with each animal subjected to three consecutive trials to calculate mean values for traversal time and slip frequency.

Adhesive Removal Test: The adhesive removal test was a standardized behavioral assay for evaluating sensorimotor function in rodent models of neurological disorders. Allow animals to acclimate to the testing chamber for 10 min per day for three days prior to baseline testing. Conduct 3 trials pre-surgery, with inter-trial intervals ≥1 h. Perform tests at 24 h post-tMCAO surgery. Gently restrain the animal and attach tapes symmetrically. Record the total time to completely detach both tapes.

Quantification of Infarct Volume Post tMCAO Surgery: Twenty hour post surgery, the rats were anesthetized with intravenous pentobarbital sodium and euthanized, following which their brains were carefully extracted. The brains were then frozen at  $-20\,^{\circ}\text{C}$  and sectioned into slices of  $\approx\!2$  mm in thickness. These sections were immersed in 1% TTC solution for 30 min to facilitate staining. High-resolution digital images of the stained sections were captured using a professional camera and analyzed using Image] software. The infarct volume was calculated using the following formula: Infarct volume ratio = [(contralateral non-infarcted area – ipsilateral non-infarcted area)/contralateral total non-infarcted area]  $\times$  100%.

Immunofluorescence Staining: Twenty hour post-surgery, rats were anesthetized with intravenous pentobarbital sodium, and their brains were harvested. The brains were frozen at  $-20\,^{\circ}\text{C}$ , and  $10\,\mu\text{m}$  coronal sections were cut and mounted on glass slides. The slides were incubated overnight at  $4\,^{\circ}\text{C}$  with anti-CD86/CD206 antibodies (1:400) and anti-GFAP antibodies (1:200). Unbound primary antibodies were removed by washing the slides three times with PBS, followed by incubation with secondary antibodies (1:400) for  $2\,\text{h}$  at room temperature. DAPI was used as a nuclear stain. The slides were observed using a confocal laser scanning microscope (CLSM, Zeiss, LSM-900) to illustrate the anti-inflammatory efects. Additionally, for observing apoptosis in the brain, brains were fixed overnight in 4% paraformaldehyde, paraffin-embedded, sectioned, and mounted on slides. TUNEL reaction mixture and hematoxylin-eosin staining were applied, and the slides were observed under the CLSM.

Hemolysis Test: Blood was collected from the abdominal aorta of rats and placed in anticoagulant tubes. The samples were centrifuged at 3000 rpm for 20 min, and the supernatant was discarded. The red blood cells (RBCs) were washed by adding double the volume of PBS and centrifuging again until the supernatant was clear. Aliquots of 20  $\mu L$  of RBCs were incubated with 1 mL PBS-diluted test nanozyme at 37 °C for 3 h. As negative and positive controls, 1 mL of PBS and 1 mL of water were mixed with 20  $\mu L$  of RBCs, respectively. The samples were centrifuged at 3000 rpm for 15 min, and the absorbance of each supernatant was measured at 540 nm. The hemolysis rate of each sample was calculated using the following formula:

Hemolysis rate (%)

= (Sample absorbance - Negative control absorbance) /

(Positive control absorbance - Negative control absorbance)  $\times$  100%(1)

Biocompatibility Evaluation: To assess the biocompatibility of the nanozyme, major organs (heart, liver, spleen, lungs, and kidneys) were harvested from rats under deep anesthesia and stained with hematoxylin

ADVANCED
FUNCTIONAL
MATERIALS

16163028, 0, Downloaded from https://advanced.onlinelibrary.wiley.com/doi/10.1002/adfm.202520000 by Hangzhou Normal University, Wiley Online Library on [10/1/2025]. See the Terms and Conditions (https://onlinelibrary.wiley.com/term/terms/files/fi

and-conditions) on Wiley Online Library for rules of use; OA articles are governed by the applicable Creative Commons

and eosin (H&E) to observe pathological changes in the tissues. Additionally, serum was collected from rats in the T-mPDA-Cu/Se and sham groups after tail vein injection to detect blood biochemical indicators such as alanine aminotransferase (ALT) and aspartate aminotransferase (AST), observing the impact of the nanozyme on rats.

Intracranial Fluorescence: The spatiotemporal distribution characteristics of T-mPDA-Cu/Se nanoparticles in the cerebral parenchyma of ischemic stroke model mice were detected using a small-animal in vivo imaging system (IVIS Spectrum, PerkinElmer). At 24 h post tail vein injection, animals were sacrificed, and brain tissues were harvested for coronal cryosectioning (20 µm thickness). Fluorescence signals were acquired under a 695 nm excitation wavelength using the IVIS Spectrum system.

Statistical Analysis: All experiments were repeated at least three times, and data are presented as mean  $\pm$  standard deviation (S.D.). Significant differences between groups were analyzed using one-way ANOVA and Tukey's post-hoc test in GraphPad Prism 8.0. A two-tailed P value of <0.05 was considered statistically significant in all cases.

## **Supporting Information**

Supporting Information is available from the Wiley Online Library or from the author.

## Acknowledgements

Y.W. and J.X. contributed equally to this work. The authors thank the following programs for the financial support: National Natural Science Foundation of China (Nos. 22205052, 22475059), Zhejiang Provincial Natural Science Foundation of China (No. LMS25B040002), Hangzhou Leading Innovation and Entrepreneurship Team Project (No. TD2022001), the Interdisciplinary Research Project of Hangzhou Normal University (No. 2024JCXK01), and the Research Start-up Fund from Hangzhou Normal University (No. 2021QDL083).

### Conflict of Interest

The authors declare no conflict of interest.

### **Data Availability Statement**

The data that support the findings of this study are available from the corresponding author upon reasonable request.

### **Keywords**

active transport, anti-neuroinflammation, antioxidation, cascaded nanozymes, cerebral ischemia reperfusion injury

Received: July 31, 2025 Revised: September 17, 2025 Published online:

- [1] V. Saini, L. Guada, D. R. Yavagal, Neurology 2021, 97, S6.
- [2] A. Avan, H. Digaleh, M. Di Napoli, S. Stranges, R. Behrouz, G. Shojaeianbabaei, A. Amiri, R. Tabrizi, N. Mokhber, J. D. Spence, BMC Med. 2019, 17, 191.
- [3] V. L. Feigin, M. O. Owolabi, F. Abd-Allah, R. O. Akinyemi, N. V. Bhattacharjee, M. Brainin, J. Cao, V. Caso, B. Dalton, A. Davis, *Lancet Neurol.* 2023, 22, 1160.

- [4] P. Khatri, D. O. Kleindorfer, T. Devlin, R. N. Sawyer, M. Starr, J. Mejilla, J. Broderick, A. Chatterjee, E. C. Jauch, S. R. Levine, JAMA 2018, 320, 156.
- [5] G. Tsivgoulis, A. H. Katsanos, E. C. Sandset, G. Turc, T. N. Nguyen, A. Bivard, U. Fischer, P. Khatri, *Lancet Neurol.* 2023, 22, 418.
- [6] C. Qin, S. Yang, Y.-H. Chu, H. Zhang, X.-W. Pang, L. Chen, L.-Q. Zhou, M. Chen, D.-S. Tian, W. Wang, Signal Transduct Target Ther. 2022, 7, 215.
- [7] P. Hernansanz-Agustín, C. Choya-Foces, S. Carregal-Romero, E. Ramos, T. Oliva, T. Villa-Piña, L. Moreno, A. Izquierdo-Álvarez, J. D. Cabrera-García, A. Cortés, *Nature* 2020, 586, 287.
- [8] Y. Huang, Z. Du, K. Li, W. Jing, P. Wei, B. Zhao, Y. Yu, Q. Cai, X. Yang, Adv. Fiber Mater. 2022, 4, 894.
- [9] H. Lu, S. Li, D. Dai, Q. Zhang, Z. Min, C. Yang, S. Sun, L. Ye, C. Teng, X. Cao, Acta Biomater. 2022, 147, 314.
- [10] F. Zeng, Y. Wu, X. Li, X. Ge, Q. Guo, X. Lou, Z. Cao, B. Hu, N. J. Long, Y. Mao, Angew. Chem., Int. Ed. 2018, 130, 5910.
- [11] B. Zhang, W. M. Bailey, A. L. McVicar, J. C. Gensel, *Neurobiol. Aging.* 2016. 47, 157.
- [12] Y. Fu, Q. Liu, J. Anrather, F.-D. Shi, Nat. Rev. Neurol. 2015, 11, 524.
- [13] A. Flemming, Nat. Rev. Immunol. 2019, 19, 473.
- [14] M. Enomoto, A. Endo, H. Yatsushige, K. Fushimi, Y. Otomo, *Stroke* 2019, 50, 652.
- [15] M. Fidalgo, J. R. Pires, I. Viseu, P. Magalhaes, H. Gregorio, V. Afreixo, T. Gregorio, Clin. Neurol. Neurosur. 2022, 219, 107299.
- [16] Q. Bao, P. Hu, Y. Xu, T. Cheng, C. Wei, L. Pan, J. Shi, ACS Nano 2018, 12, 6794.
- [17] R. Tian, H. Ma, W. Ye, Y. Li, S. Wang, Z. Zhang, S. Liu, M. Zang, J. Hou, J. Xu, Adv. Funct. Mater. 2022, 32, 2204025.
- [18] J. Song, G. Yang, Y. Song, Z. Jiang, Y. Jiang, Y. Luan, W. He, Adv. Funct. Mater. 2024, 34, 2315275.
- [19] D. Wu, J. Zhou, Y. Zheng, Y. Zheng, Q. Zhang, Z. Zhou, X. Chen, Q. Chen, Y. Ruan, Y. Wang, Nat. Commun. 2023, 14, 7147.
- [20] Z. Wang, Y. Zhao, Y. Hou, G. Tang, R. Zhang, Y. Yang, X. Yan, K. Fan, Adv. Mater. 2024, 36, 2210144.
- [21] Y. Liu, G. Li, T. Zhang, Y. Wu, K. Hu, C. Wu, X. Dai, W. Feng, Y. Chen, Adv. Mater. 2025, 37, 2503576.
- [22] Y. Du, Y. Huo, Q. Yang, Z. Han, L. Hou, B. Cui, K. Fan, Y. Qiu, Z. Chen, W. Huang, J. Lu, L. Cheng, W. Cai, L. Kang, Exploration 2023, 3, 20220041.
- [23] Y. Liu, Y. Cheng, H. Zhang, M. Zhou, Y. Yu, S. Lin, B. Jiang, X. Zhao, L. Miao, C.-W. Wei, Sci. Adv. 2020, 6, abb2695.
- [24] G. C. Terstappen, A. H. Meyer, R. D. Bell, W. Zhang, *Nat. Rev. Drug Discovery* 2021, 20, 362.
- [25] Z. W. Du, Y. S. Li, X. C. Jiang, J. Q. Gao, Small 2025, 21, 2410404.
- [26] L. He, G. Huang, H. Liu, C. Sang, X. Liu, T. Chen, Sci. Adv. **2020**, 6, aay9751.
- [27] S. Wang, X. Shi, T. Xiong, Q. Chen, Y. Yang, W. Chen, K. Zhang, Y. Nan, Q. Huang, K. Ai, Adv. Mater. 2024, 36, 2409529.
- [28] Y. Liu, K. Ai, X. Ji, D. Askhatova, R. Du, L. Lu, J. Shi, J. Am. Chem. Soc. 2017, 139, 856.
- [29] R. Prakash, A. Vyawahare, R. Sakla, N. Kumari, A. Kumar, M. M. Ansari, Kanika, C. Jori, A. Waseem, A. J. Siddiqui, M. A. Khan, A. A. B. Robertson, R. Khan, S. S. Raza, ACS Nano 2023, 17, 8680.
- [30] Z. Chai, X. Hu, X. Wei, C. Zhan, L. Lu, K. Jiang, B. Su, H. Ruan, D. Ran, R. H. Fang, J. Control. Release 2017, 264, 102.
- [31] Y. Zou, Y. Liu, Z. Yang, D. Zhang, Y. Lu, M. Zheng, X. Xue, J. Geng, R. Chung, B. Shi, Adv. Mater. 2018, 30, 1803717.
- [32] L. Peng, H. Peng, W. Li, D. Zhao, Nat. Protoc. 2023, 18, 1155.
- [33] L. Peng, C.-T. Hung, S. Wang, X. Zhang, X. Zhu, Z. Zhao, C. Wang, Y. Tang, W. Li, D. Zhao, J. Am. Chem. Soc. 2019, 141, 7073.
- [34] J. Li, K. Li, D. Shao, Y. Ding, L. Huang, X. Zheng, Appl. Surf. Sci. 2023, 613, 155950.
- [35] J. A. Tainer, E. D. Getzoff, J. S. Richardson, D. C. Richardson, *Nature* 1983, 306, 284.



www.advancedsciencenews.com



www.afm-journal.de

16163028, 0, Downloaded from https://advanced.onlinelibrary.wiley.com/doi/10.1002/adfm.202520000 by Hangzhou Normal University, Wiley Online Library on [10/11/2025]. See the Terms

on Wiley Online Library for rules of use; OA articles are governed by the applicable Creative Commons

- [36] Z. Xiong, G. Huang, J.-R. Huang, Y. Liu, L. He, T. Chen, Nat. Commun. 2025, 16, 8030.
- [37] Y. Liu, R. Huang, L. Han, W. Ke, K. Shao, L. Ye, J. Lou, C. Jiang, Biomaterials 2009, 30, 4195.
- [38] R. Wang, R. Xiao, Z. Zeng, L. Xu, J. Wang, Int. J. Nanomed. 2012, 7, 4185
- [39] Q. Z. Tuo, S. T. Zhang, P. Lei, Med. Res. Rev. 2022, 42, 259.
- [40] R. Mao, N. Zong, Y. Hu, Y. Chen, Y. Xu, Neurosci. Bull. 2022, 38, 1229.
- [41] Y. Li, J. Liao, L. Xiong, Z. Xiao, F. Ye, Y. Wang, T. Chen, L. Huang, M. Chen, Z.-S. Chen, J. Control Release 2024, 368, 607.
- [42] Y. Liu, Y. Zhang, Q. Liu, Q. Wang, A. Lin, J. Luo, Y. Du, Y.-W. Lin, H. Wei, Analyst 2021, 146, 1872.
- [43] J. Niu, S. Sun, P. Liu, X. Zhang, X. Mu, J. Inorg. Mater. 2023, 38, 489.

- [44] Q. Ren, Z. Hu, Y. Jiang, X. Tan, B. O. Botchway, N. Amin, G. Lin, Y. Geng, M. Fang, Front. Neurol. 2019, 10, 1289.
- [45] L. Liu, J. Yao, Z. Li, G. Zu, D. Feng, Y. Li, W. Qasim, S. Zhang, T. Li, H. Zeng, Cell Death Dis. 2018, 9, 411.
- [46] J. P. Crow, Methods Enzymol. 1999, 301, 151.
- [47] D. Amantea, G. Bagetta, Curr. Opin. Pharmacol. 2017, 35, 111.
- [48] E. Z. Longa, P. R. Weinstein, S. Carlson, R. Cummins, Stroke 1989, 20, 84.
- [49] T. Schallert, S. M. Fleming, J. L. Leasure, J. L. Tillerson, S. T. Bland, Neuropharmacology 2000, 39, 777.
- [50] X. Shi, H. Bai, J. Wang, J. Wang, L. Huang, M. He, X. Zheng, Z. Duan, D. Chen, J. Zhang, Front. Neurol. 2021, 12, 667511.
- [51] Z. Ding, X. Liu, H. Jiang, J. Zhao, S. Temme, P. Bouvain, C. Alter, P. Rafii, J. Scheller, U. Flögel, Sci. Rep. 2024, 14, 25214.
- [52] M. K. Jha, S. Jeon, K. Suk, Immune Netw. 2012, 12, 41.